JOURNAL OF MECHANICAL ENGINEERING AND SCIENCES
ISSN: 2289-4659 e-ISSN: 2231-8380
VOLUME 19, ISSUE 4, 2025, 10845 - 10862
DOI: https://doi.org/10.15282/jmes.19.4.2025.2.0850

RESEARCH ARTICLE

Insights into hydrogen bubble dynamics and electrochemical performance on flat and electrochemically etched stainless steel electrodes using high-speed imaging

Waqad Ul Mulk[1,2]*, A. Rashid A. Aziz[1,2], Asghar Ali Ghoto[2,3], Rabia Khatoon[4], Mhadi A. Ismael[5], Mior A. Said[1,2]

[1] Center of Sustainable Resources and Efficient Mobility (CSRIEM), Universiti Teknologi Petronas, 32610, Bandar Seri Iskandar, Perak, Malaysia
[2] Department of Mechanical Engineering, Universiti Teknologi Petronas, 32610, Bandar Seri Iskandar, Perak, Malaysia
[3] Mechanical Engineering Department, MUET SZAB Campus Khairpur Mir's, 66020, Pakistan
[4] Department of Civil Engineering, The University of Larkano, Airport Road Larkano, Sindh 77150, Pakistan
[5] Interdisciplinary Research Center for Hydrogen Technologies and Carbon Management (IRC-HTCM), King Fahd University of Petroleum & Minerals, Dhahran, 31261, Saudi Arabia

ABSTRACT - Gas bubbles formed on electrodes during electrochemical processes increase overpotential and ohmic voltage drop, leading to higher energy consumption in water electrolysis. This study investigates the effect of surface roughness on hydrogen bubble dynamics and hydrogen evolution reaction (HER) performance using flat and electrochemically etched SS-316L working electrodes. Electrochemical experiments were conducted at room temperature in a three-compartment acrylic cell using a potentiostat. The SS-316L electrodes served as the working electrode (WE), with platinum and Ag/AgCl wires functioning as the counter and reference electrodes in 0.5 M KOH electrolyte. The etched electrode was prepared through electrochemical etching in a freshly prepared dilute Aqua Regia solution, followed by ultrasonic cleaning and drying. Bubble evolution was recorded using a high-speed visualization system. Results reveal that the etched electrode exhibits smaller bubble detachment radii (average 162 µm vs. 248 µm), shorter growth time (5.8 s vs. 9.2 s), and lower voltage fluctuations than the flat electrode, indicating improved bubble release dynamics. Enhanced surface roughness promotes higher HER activity, with the etched electrode showing a reduced onset potential of 0.43 V (0.11 V lower than flat WE), decreased overpotential from 331.4 to 247.8 mV at 10 mA cm^{-2}, and a lower charge transfer resistance (67.2 Ω vs. 234.3 Ω). The double-layer capacitance increases from 0.38 to 0.91 mF cm^{-2}, confirming a larger electrochemically active surface area. The etched electrode also demonstrates superior stability, maintaining consistent polarization behaviour after 500 CV cycles at 100 mV s^{-1}.

ARTICLE HISTORY
Received : 2nd Aug. 2025
Revised : 26th Oct. 2025
Accepted : 28th Oct. 2025
Published : 29th Dec. 2025

KEYWORDS
Electrochemically etched electrode
H_2 bubbles dynamics
High-speed camera analysis
Stainless steel

1. INTRODUCTION

Hydrocarbons remain the dominant conventional energy source, but their combustion in vehicles and power generation systems releases hazardous gases, intensifying environmental concerns. This has heightened global efforts to mitigate pollution and transition toward renewable energy solutions [1-3]. Hydrogen (H_2) has emerged as a key player in the green economy, serving as a clean and sustainable energy carrier that can significantly reduce carbon emissions and facilitate the shift toward renewable energy sources [4, 5]. H_2 can be produced through various pathways, including steam methane reforming (SMR), coal gasification, biomass gasification, and electrochemical water splitting. Among these, SMR is the most widely adopted due to its low production cost and high efficiency [6, 7]. However, despite its economic advantages, SMR has several drawbacks, including its energy-intensive nature, limited operational flexibility, and heavy reliance on fossil fuels, which results in substantial carbon emissions [8].

Electrochemical water splitting is a promising approach for producing green H_2, making it essential to enhance the H_2 evolution reaction (HER) for optimal energy utilization. During this process, electrochemical reactions occur at active sites of the electrode surface, producing H_2 molecules. As these molecules accumulate, they form bubbles due to oversaturation, which grow until they reach a critical size and detach from the electrode [9, 10]. Studies on electrochemical water splitting using a flow-through configuration have shown that bubble accumulation on the electrode surface negatively impacts process efficiency. These bubbles reduce the available active surface area and obstruct ion transport pathways, leading to increased overpotential and resistance at the electrode interface [11]. Furthermore, hydrodynamic analyses indicate that regions beneath the bubbles do not actively contribute to electrode reactions, effectively decreasing the effective reaction area. This reduction forces a higher actual current density on the remaining active sites, contributing to a screening effect that further limits HER performance [12].

For an efficient electrolysis process, the rapid removal of generated bubbles from active sites is essential to maximize the surface area for gas evolution reactions. One of the key strategies to enhance bubble detachment involves the application of external fields, which introduce extra driving forces to enhance bubble detachment. Magnetic [13] and

*CORRESPONDING AUTHOR | W.U. Mulk | ✉ Waqad_22010090@utp.edu.my

ultrasonic fields [14] induce forced convection within the electrolyte, while hypergravity fields [15] enhance bubble buoyancy, promoting faster detachment from both the electrode surface and the electrolyte. However, these techniques come with drawbacks, as they require additional accessories, increasing system complexity and cost, which pose challenges for large-scale applications. Recent research has highlighted the significant influence of wettability on bubble dynamics, showing that even slight variations in hydrophilicity can significantly affect bubble behaviour [16]. Although these findings provide valuable insights, additional research on fundamental chemical interactions and the careful selection of electrode materials is essential for a deeper understanding and practical implementation.

Another effective approach to enhancing bubble detachment in electrochemical processes involves optimizing the electrode structure. The shape and design of electrodes play a critical role in determining the electrochemical active surface area (ECSA) and have a significant impact on bubble formation and transport dynamics [17]. Surfaces featuring nanostructures like nanoarrays [18], nanosheets [19], and nanocones [20] create a discontinuous gas-liquid-solid interface, reducing bubble adhesion and enabling smaller bubble detachment [21]. For example, Li *et al.* [22] developed a superaerophobic pine-shaped Pt nanoarray electrode that reduced adhesive force by approximately 13 times and decreased bubble size by nearly sixfold compared to a flat Pt electrode. Similarly, Kim *et al.* [23] developed a Mo-doped CoP electrode with a sprout-shaped structure, incorporating nanoarray-type pillars with microscale tips, which significantly enhanced bubble release efficiency. However, while nanostructured electrodes minimize adhesive forces, those with extremely low hydrophilicity can hinder bubble detachment, leading to bubble accumulation and increased overpotential. Additionally, fabricating these intricate nanostructures uniformly on a large scale remains a major challenge, limiting their widespread practical implementation [24]. Beyond nanostructures, researchers have explored various innovative catalytic materials with distinct architectures, such as hierarchical designs [25], open finger-like holes [26], and caterpillar-like structures [27]. However, most studies primarily focus on the catalytic performance of these materials, with comparatively less attention given to how electrode structure influences bubble dynamics. A deeper understanding of the interplay between electrode morphology and bubble behaviour is essential for optimizing electrochemical hydrogen production efficiency.

Stainless steel (SS) is extensively used in water electrolysis systems due to its superior mechanical strength, corrosion resistance, and cost-effectiveness. As an electrode material, SS provides a robust substrate for HER and OER catalysts, particularly in alkaline and AEMWE systems. Its surface properties can be modified to enhance catalytic activity and facilitate gas bubble detachment through mechanical and chemical treatments such as grinding, sandblasting, and chemical-electrochemical etching. Several researchers have explored different modification techniques for stainless steel. For instance, Alhakemy *et al.* [28] modified SS electrodes by depositing nickel phosphide (NiP) nanoparticles through one-step electrodeposition, resulting in a binder-free, non-precious electrode for AWE. By optimizing the deposition time, they achieved a highly porous and homogeneous surface morphology, which significantly improved the ECSA and catalyst-substrate interaction. The optimized xNiP@SS electrode showed higher catalytic performance, with overpotentials of 238 mV (OER, 10 mA cm^{-2}) and 268 mV (HER, 10 mA cm^{-2}), along with Tafel slopes of 41.24 mV dec^{-1} and 70.5 mV dec^{-1}, respectively.

Similarly, Sultana *et al.* [29] developed an electrochemical conditioning method combined with galvanic replacement using 0.5 wt.% gold nanoparticles to enhance the electrocatalytic performance of SS (AISI 316) for overall water splitting. The modified electrode demonstrated outstanding OER activity with a low Tafel slope of 29 mV dec^{-1} and achieved high HER performance, sustaining current densities of 100 mA cm^{-2}. Lavorante *et al.* [30] investigated the performance of various surface-modified SS 316L electrodes in AWE. These included untreated electrodes, chemically pickled ones, and mechanized electrodes with a straight-parallel topology. Experiments were conducted with 5.3 mm and 6.1 mm electrode spacings, revealing that the larger spacing reduced bubble resistance and enhanced performance. Among the tested configurations, the mechanized electrodes with a straight-parallel topology exhibited the best results, increasing the active surface area by 50% and achieving a corresponding boost in current density. Similarly, Zeng *et al.* [31] explored surface modification techniques to minimize reaction resistance. They employed mechanical polishing with sandpapers of different grits (P400, P2000, P4000) and electrochemical deposition of Ni and Co to achieve varied surface roughness. Among the tested electrodes, the P400-polished electrodes demonstrated the best performance, exhibiting lower overpotential and an increased surface area.

Previous experimental work has shown that electrochemical etching and activation can convert stainless steel into a more active, porous electrocatalyst by increasing surface roughness, porosity and charge-transfer efficiency, which enhances HER current densities [32]. Experimental studies on porous electrodes also demonstrate that increased pore volume and optimized pore structure boost specific surface area and improve gas release and mass transport, leading to lower overpotentials and better HER performance compared with solid electrodes [33]. In parallel, high-speed imaging studies of gas-evolving electrodes have experimentally shown how bubble nucleation, growth and detachment dynamics depend strongly on surface morphology and operating conditions, and how these bubble processes directly impact local current/voltage fluctuations and effective active area [14]. However, systematic studies correlating electrochemical etching–induced surface morphology with real-time hydrogen bubble dynamics and HER performance remain limited.

This study addresses this gap by examining the influence of electrochemical etching on hydrogen bubble behaviour and HER activity through high-speed imaging, an area that has not been extensively explored in the literature. We prepared a surface-modified electrode using SS-316L via an electrochemical etching process by immersing the sample in

a dilute Aqua Regia solution (HCl + HNO_3) and applying a constant electric potential of 10 V for 15 min. The findings revealed that electrochemical etching significantly affected bubble dynamics and HER activity. The etched WE exhibited lower bubble radii and growth time than the flat WE, along with reduced voltage fluctuations, indicating improved bubble detachment. The micropores on the electrode surface led to more active sites with higher bubble production efficiency. Electrochemical measurements including linear sweep voltammetry (LSV), electrochemical impedance spectroscopy (EIS), cyclic voltammetry (CV), electrochemical active surface area (ECSA) evaluation, and long-term stability tests further highlighted the enhanced HER activity of the etched WE.

2. MATERIALS AND METHODS

2.1 Materials

Electrochemical experiments were performed at room temperature using a three-compartment acrylic cell and a potentiostat (METROHM LTD, Herisau, Switzerland) following the protocol outlined in this study [34]. Stainless steel SS-316L (TSA Industries Sdn Bhd., Malaysia) with dimensions (20×20×1.0 mm) served as the working electrode (WE), with platinum wire (100×0.5 mm) and Ag/AgCl wire (100×1.0 mm) functioning as the counter electrode (CE) and reference electrode (RE), respectively. The electrolyte consisted of 0.5 M KOH, prepared using KOH pellets (ACS reagent, Sigma-Aldrich) dissolved in deionized (DI) water. Hydrochloric and Nitric acids (Luli Chemical Co., Ltd) were used to prepare the Aqua Regia solution.

2.2 Electrode Preparation

A dilute Aqua Regia solution was prepared by mixing 2.5% (1 N) HCl (55% ACS reagent Sigma-Aldrich) and 1.5% HNO_3 aqueous solutions (70% ACS reagent Sigma-Aldrich) in a 1:1 volume ratio. To prevent decomposition from rapid self-dissociation, the solution was freshly prepared before the experiments [35]. A 20 mm × 20 mm × 1.0 mm SS-316L specimen served as the target material. It was positioned parallel to a 0.5 mm Pt wire, maintaining a 50 mm separation. The SS specimen was connected to the anode, while the Pt wire served as the cathode. Both were immersed in the Aqua Regia solution, and a voltage of 10 V was applied for 15 min to initiate electrochemical etching. After etching, the sample was subsequently sonicated in ethanol for 30 min, followed by drying in an electric oven at 80 °C for 15 min to prepare it for the subsequent electrochemical experiments. The schematic of the SS-316L electrochemical etching and post-etching treatment is illustrated in Figure 1.

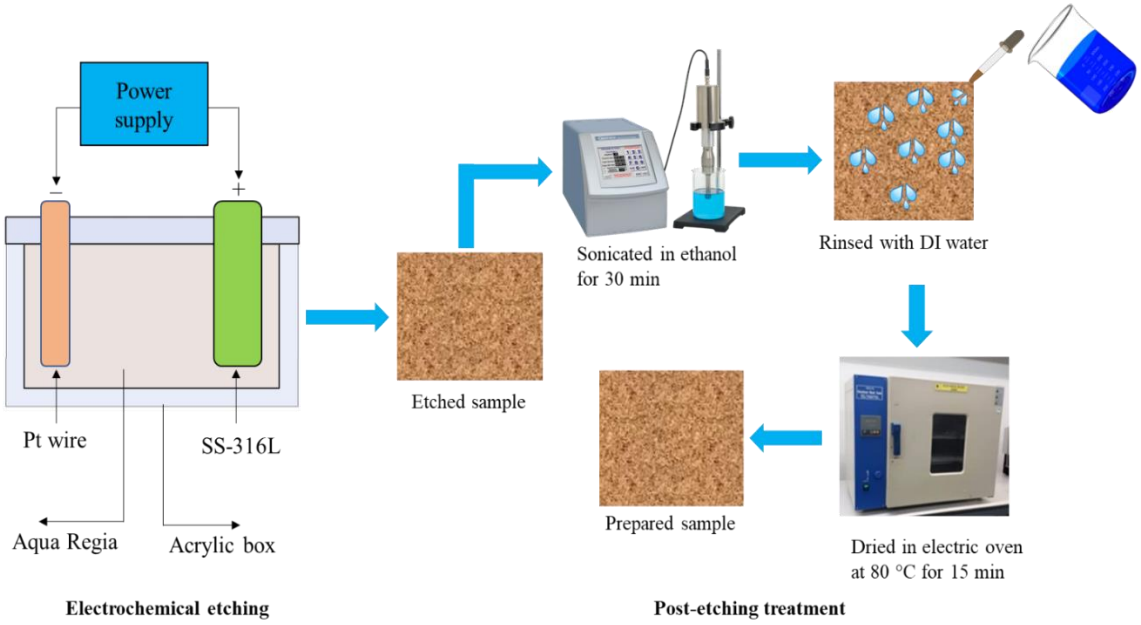

Figure 1. Preparation of electrode through electrochemical etching process

2.3 Characterization and Analysis

The current study used a metallographic microscope (Leica DM1000-3000) to observe the microstructure characterization of the electrodes under different magnifications. Atomic force microscopy (AFM-Nanonavi Esweep) was used to find the roughness parameters of both electrodes. Both the WEs were cut into 1 x 1 cm^2 square shapes, according to the requirement of the AFM testing machine. A high-speed camera (8001-Phantom Miro M310, USA) with a high-resolution microscope (K2, Boulder, CO, USA) and a zoom lens type CF3 objective was used to visualize the H_2 bubbles during growth and detachment stages. The camera was operated at 4000 fps, with a frame interval of 170.20 µs and an exposure time of 25 µs. The imaging system featured a resolution of 320 × 240 pixels with a scale factor of 0.195 µm/pixel.

2.4 Experimental Setup

Figure 2 illustrates the schematic setup for the H_2 bubbles visualization and electrochemical performance. All the electrodes were enclosed in a transparent acrylic box with 0.5 M KOH electrolyte. The electrodes were connected to a potentiostat having a range of 0.01-12 V and 0.01-15 A, allowing operation at different operating conditions. A multi-LED light source (LT-V8-15, Tokyo, Japan) was used to maintain consistent lighting during electrolysis. The high-speed camera was connected to a PC to control and monitor key real-time parameters, such as frame rate, exposure time, and resolution.

2.5 Image Processing

In previous studies, most researchers have employed ImageJ software to measure the bubble size [36, 37]. Herein, we employed a MATLAB algorithm to detect the bubbles with accurate size. The code utilized the "imfindcircles" function to identify circular objects in images. The program first retrieves images from a specified location. It then identifies circular objects by analyzing their centers, radii, and metric values. The pixel readings are subsequently transformed into micrometers by applying a predetermined scale factor of 0.195 µm/pixel. The image processing technique proved to be highly effective in identifying bubbles as presented in Figure 3, evident from the substantial number of detected bubbles and their distribution.

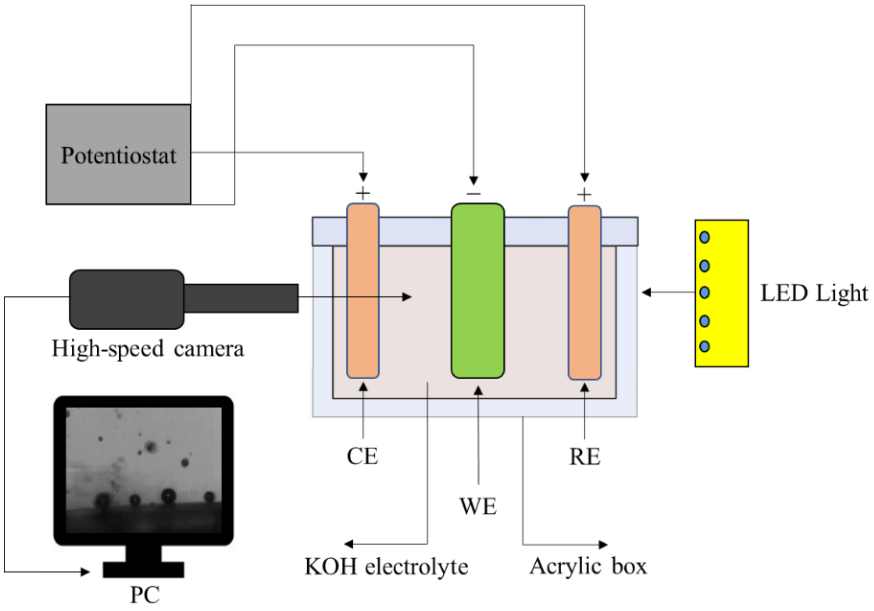

Figure 2. Experimental setup for bubbles visualization and electrochemical performance

2.6 Hydrogen Bubble Kinetics

The lifetime of a surface-bound bubble can be divided into three distinct stages: nucleation, growth, and detachment. At the start of electrolysis, the gas molecules produced at electrodes initially dissolve in the electrolyte. As gas supersaturation increases, conditions become favorable for bubble nucleation, initiating subsequent bubble growth [38]. Bubble growth kinetics are well established and are typically characterized by Scriven's theory, as presented in Eq. 1 [39].

$$R_b = \beta t_b^{\alpha} \tag{1}$$

Here, r_b represents the bubble radius, β is the growth coefficient, t_b denotes the time since nucleation, and α is the time exponent. Bubble growth follows three distinct regimes depending on the value of α. In the pressure-driven regime (α=1), the r_b increases linearly with time. When the bubble grows on an electrode surface significantly larger than its detachment size, the growth transitions to a diffusion-limited regime (α=1/2) [40]. Conversely, a reaction-limited regime prevails when gas production is localized at the base of the bubble, a phenomenon commonly observed with micro and nano-electrodes [41]. In this regime, the gas produced at the electrode is almost entirely absorbed into the bubble, mainly through the coalescence of smaller microbubbles. Consequently, under constant current conditions, the bubble expands at a uniform volumetric rate (α=1/3) [42].

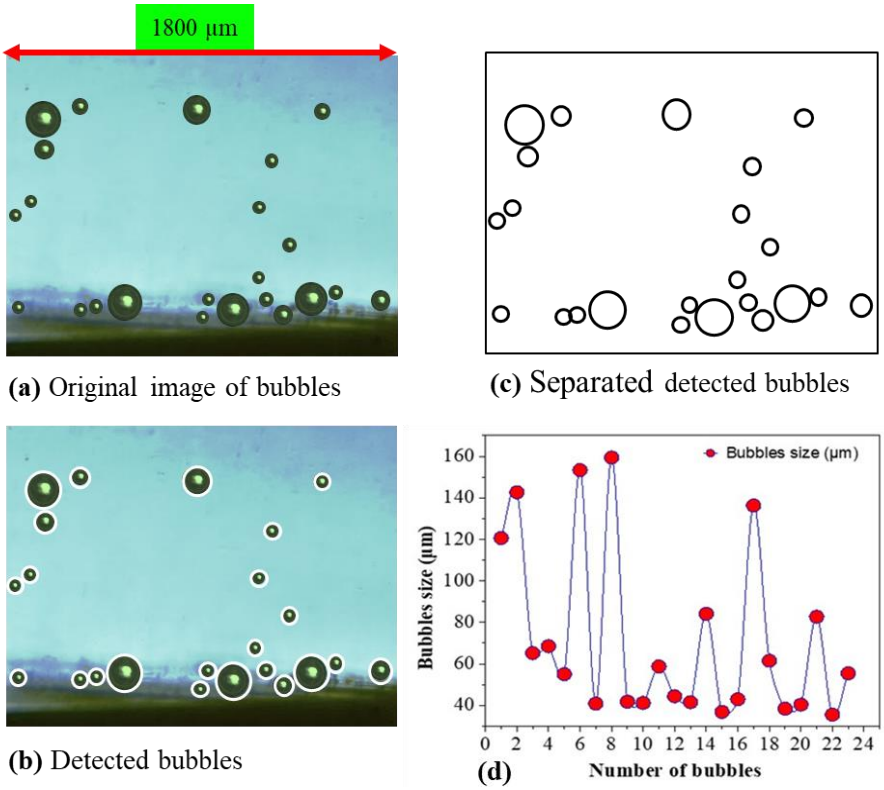

Figure 3. Image processing and analysis of H_2 bubbles with a scale bar using the MATLAB program

2.7 Bubbles Production Efficiency

The H_2 bubbles production rate is a key indicator of the efficiency of electrolysis systems and is primarily influenced by the surface characteristics of the electrode. Properties such as surface roughness and the electrochemically active surface area play a significant role in determining how H_2 bubbles nucleate, grow, and detach. These factors, in turn, impact mass transport during the electrolysis process, as excessive bubble accumulation can create resistance, reducing the overall performance of the system. In this study, we experimentally investigated the H_2 bubble production rate over time for both flat and electrochemically etched WEs. The experiments were conducted at a constant current density of 10 mA cm^{-2} to maintain consistent operational conditions. To ensure a comprehensive analysis, we examined five distinct active sites on each electrode, where bubbles of different sizes were generated. By recording and analyzing the bubble production data, we calculated the number of bubbles produced per minute and identified which electrode exhibited the highest production rate. Additionally, we observed that the etched electrode, with its enhanced surface roughness and larger electrochemically active surface area, facilitated more efficient bubble detachment, minimizing blockages and improving mass transfer. These findings highlight the importance of electrode surface engineering in optimizing bubble dynamics, which is critical for advancing the efficiency and scalability of electrolysis systems for efficient H_2 production.

2.8 Electrochemical Performance

Electrochemical measurements were conducted at room temperature in a three-electrode setup. SS-316L served as the WE, while a platinum and Ag/AgCl wire as the CE and RE, respectively. The HER catalytic activity of both WEs was evaluated through LSV. Initially, LSV measurements were recorded relative to the Ag/AgCl RE and then converted to the RHE scale to determine the electrode overpotentials. The conversion was performed based on Eq. (2) [43].

$$E_{RHE} = E_{Ag/AgCl} + E^{0}_{Ag/AgCl} + 0.059 \bullet pH \quad (1)$$

Here, E_{RHE} denotes the potential relative to RHE, whereas $E_{Ag/AgCl}$ represents the potential measured against the Ag/AgCl RE. The term $E^{0}_{Ag/AgCl}$ refers to the standard potential of the Ag/AgCl RE, typically 0.197 V. The variable pH corresponds to the pH level of the electrolyte (14.0 for 0.5 M KOH) used in the measurement.

The LSV was performed over a converted voltage range of 0 to -0.7 V vs. RHE at a scan rate of 10 mV/s. The Tafel slopes were obtained by plotting the LSV data using the Tafel equation, providing insights into the reaction kinetics. EIS was employed to investigate the electrical properties of the WEs under varying voltage conditions. The EIS was performed at an overpotential of 200 mV with a low and high frequency of 0.01 and 100 kHz. The ECSA was estimated from the Cdl vs. scan rate at 0.15 V vs. RHE (Δj= 0.15 V). Additionally, chronopotentiometry was applied to evaluate the durability of the electrochemically etched WE with 500 CV cycles.

3. RESULTS AND DISCUSSION

3.1 Surface Morphologies and Roughness Profiles

Figure 4(a) illustrates the microstructure of SS-316L observed at 50X magnification, revealing distinct grain boundaries. For a detailed analysis, the scaled images captured with the metallographic microscope were processed using ImageJ software to determine grain size via the line intercept method. A total of 70 grains were measured and the results were presented as a histogram with a bell curve, as shown in Figure 4(b), to calculate the average grain size. The smallest and largest grain sizes were 4.0 µm and 9.0 µm, respectively, with the majority of grains falling in the 6.0–7.0 µm range. The average grain size was determined to be 6.44 µm.

The surface morphologies of flat and electrochemically etched WEs demonstrate notable differences. As shown in Figure 4(a), the flat WE at a magnification of 50X exhibits a polished and homogeneous morphology. This smoothness arises from mechanical polishing, which minimizes surface irregularities, resulting in a lower surface roughness and a limited effective surface area. Such characteristics make the flat surface less interactive with its environment, reducing its suitability for electrochemical applications that depend on high surface activity [44]. In contrast, as shown in Figure 4(c) and Figure 4(d), the electrochemically etched WE shows a highly roughened surface with microscale pores and bumps. This observation aligns with the findings of Lee *et al.* [35] and Ban *et al.* [45], who reported that SS substrates etched at 10 V for 10 min displayed both nanopores and microscale bumps, resulting in a hierarchical surface structure and a notable change in wettability. These features result from selective material dissolution during the etching process, which preferentially removes material at grain boundaries and weak points in the microstructure. This process creates a significantly rougher surface with prominent peaks and valleys, substantially increasing the effective surface area and introducing a micro-textured topology. The structural changes enhance the functional properties of the surface, making it more suitable for applications that benefit from improved wettability, stronger adhesion, or higher catalytic activity, such as in electrochemical applications where high surface area facilitates better interaction with electrolytes and enhances the electrochemical activity [46].

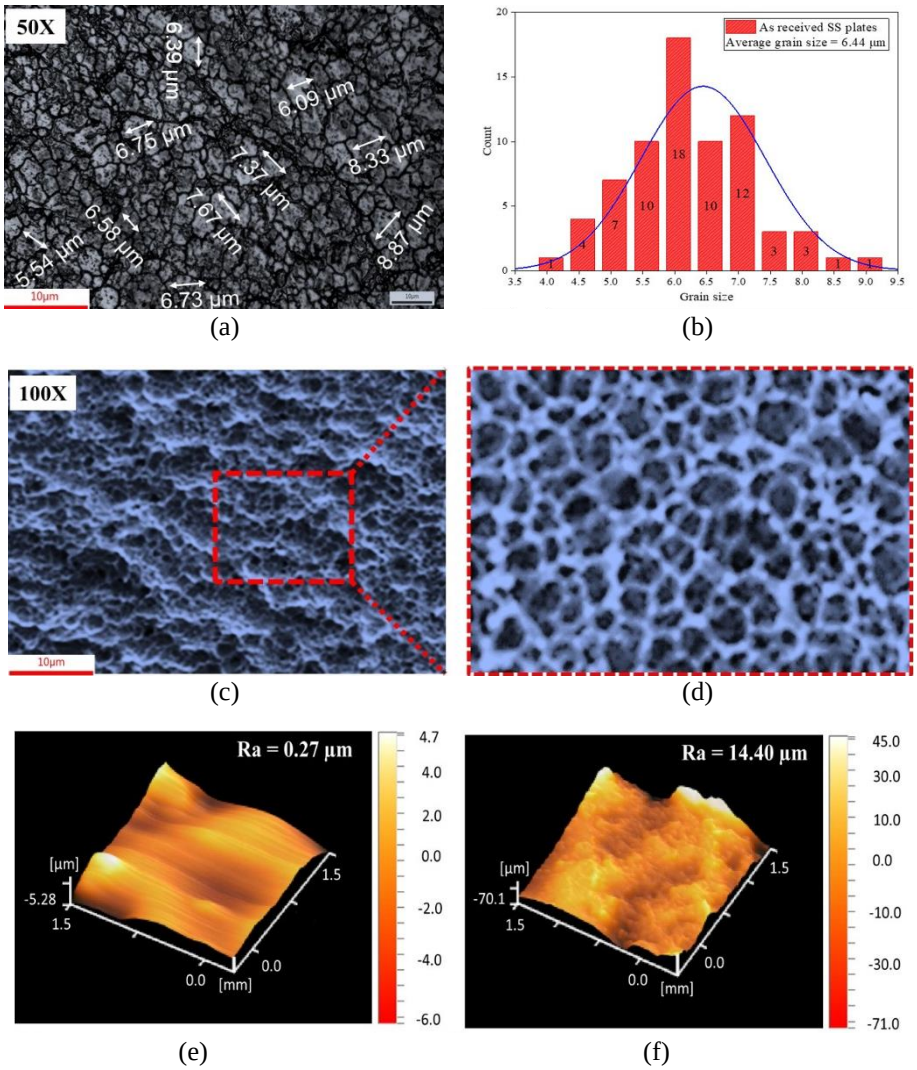

Figure 4. (a, b) Grain size distribution of the as-received SS. (c, d) Surface morphology of the electrochemically etched SS at 10 V for 15 min at 100X magnification. Surface topography of (e) Flat WE and (f) Electrochemically etched WE

The 3D surface plot for the Flat WE in Figure 4(e) shows a relatively smooth surface with an average roughness (Ra) of 0.27 µm. The electrochemical etching has significantly increased the average roughness of the stainless steel. As shown in Figure 4(f), the Ra of the etched WE is increased to 14.40 µm. This is consistent with previous literature, where electrochemical etching of stainless steel was shown to enhance surface roughness for applications such as oil retention [35]. The increased roughness with microporous structure plays a vital role in improving HER activity. The rough and microporous surface provides a larger active area, enhances mass transport by facilitating reactant diffusion, and promotes efficient bubble release during gas evolution [47]. Additionally, electrodes with higher surface roughness and microporous features exhibit lower overpotentials and higher current densities, making them highly efficient for HER applications [48].

3.2 Hydrogen Bubble Kinetics

The influence of current density on bubble growth rate is depicted in Figure 5 and Figure 6(a, b), where r_b is plotted against t_b for a single bubble. As the current density increases, r_b grows at a faster rate, indicating that a greater amount of H_2 gas is absorbed by the bubble. Although gas evolution efficiency depends on current density, the overall bubble growth dynamics exhibit a consistent pattern across all current levels. The double logarithmic plot in Figure 6(c, d) reveals that the bubbles in this study do not follow a single power-law model $r_b \propto t_b^{\alpha}$. Instead, $r_b(t_b)$ gradually transitions from pressure-driven growth ($\alpha \approx 1$) to reaction-limited growth ($\alpha \approx 1/3$), aligning with previous studies that also observed a shift in growth regimes rather than adherence to a single model [49]. In simple terms, bubble growth begins with a pressure-driven phase ($\alpha \approx 1$), then transitions to a diffusion-limited phase ($\alpha \approx 1/2$), and eventually enters a reaction-limited growth phase ($\alpha \approx 1/3$).

Figure 6(a) shows the effect of current density on H_2 bubble evolution, representing r_b as a function of t_b for both WEs. Each curve represents the bubble's growth after nucleation to detachment. As the current density increases, r_b decreases, and the t_b curves shorten significantly. This behaviour is attributed to enhanced reaction rates and increased H_2 production at higher current densities [50, 51]. At the same current densities, the bubble growth patterns on flat and etched electrodes remain nearly identical, indicating that surface roughness does not directly impact growth behaviour. However, variations in current density and roughness parameters significantly influence bubble detachment characteristics. For instance, on a flat WE, increasing the current density from 6 to 10 mA cm^{-2} reduces the bubble detachment radius from 179 µm to 143.7 µm. A similar trend is observed for the electrochemically etched WE, as illustrated in Figure 6(b). This showed that surface roughness has progressively reduced the bubble detachment radius with a reduced bubble lifetime. The findings reveal a significant reduction in r_b with the increase in current density and electrode roughness, consistent with the trends observed in previous studies [52].

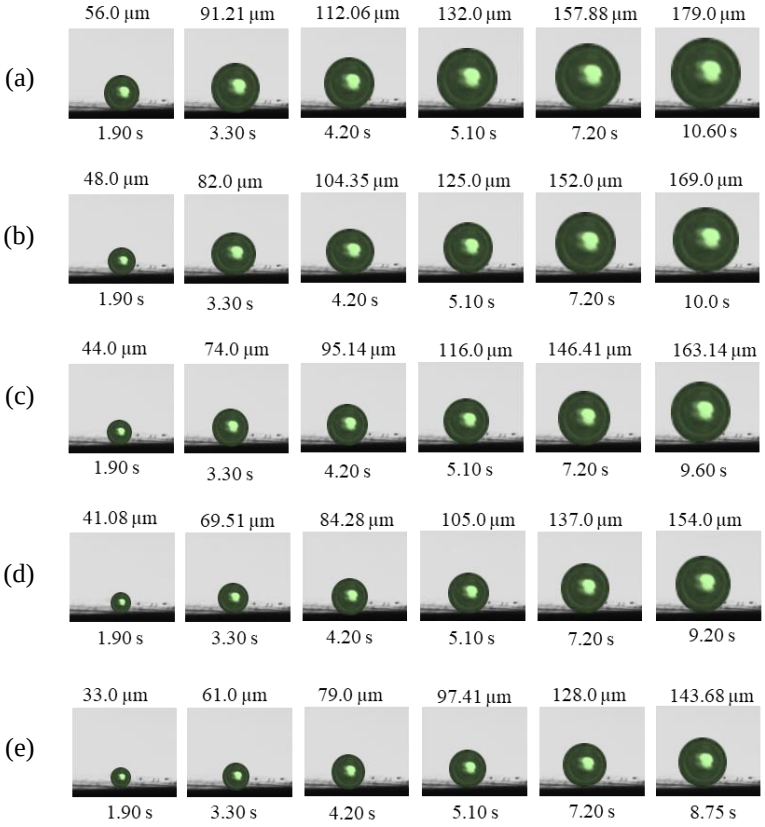

Figure 5. Bubble growth pattern vs lifetime using flat surface WE at a different current density of (a) 6.0 (b) 7.0 (c) 8.0 (d) 9.0, and (e) 10.0 mA cm^{-2}

Additionally, as shown in Figure 6(a,b), increasing the current density reduces the bubble lifetime across both WEs. For example, on a flat WE, the lifetime of a single bubble decreases from 10.60 s at 6 mA cm^{-2} to 8.75 s at 10 mA cm^{-2}. A similar trend is observed for the electrochemically etched WE, where the bubble lifetime drops from 8.5 s at 6 mA cm^{-2} to 5.9 s at 10 mA cm^{-2}. This behaviour aligns with previous studies, as lower current densities result in higher surface tension at the electrode, making bubble detachment more difficult and prolonging their residence time. In contrast, higher current densities enhance gas evolution rates due to more vigorous electrochemical reactions at the cathode, promoting faster bubble detachment [53]. The decrease in bubble detachment radius at higher current densities is attributed to mass transfer limitations and rapid gas release, which become dominant factors. The bubble formation occurs rapidly, leaving less time for the bubbles to grow before detaching from the electrode surface [54]. Furthermore, an increase in current density raises the temperature of the electrolysis process, leading to a reduction in surface tension. As a result, bubbles detach more quickly from the surface with smaller detachment radii [55].

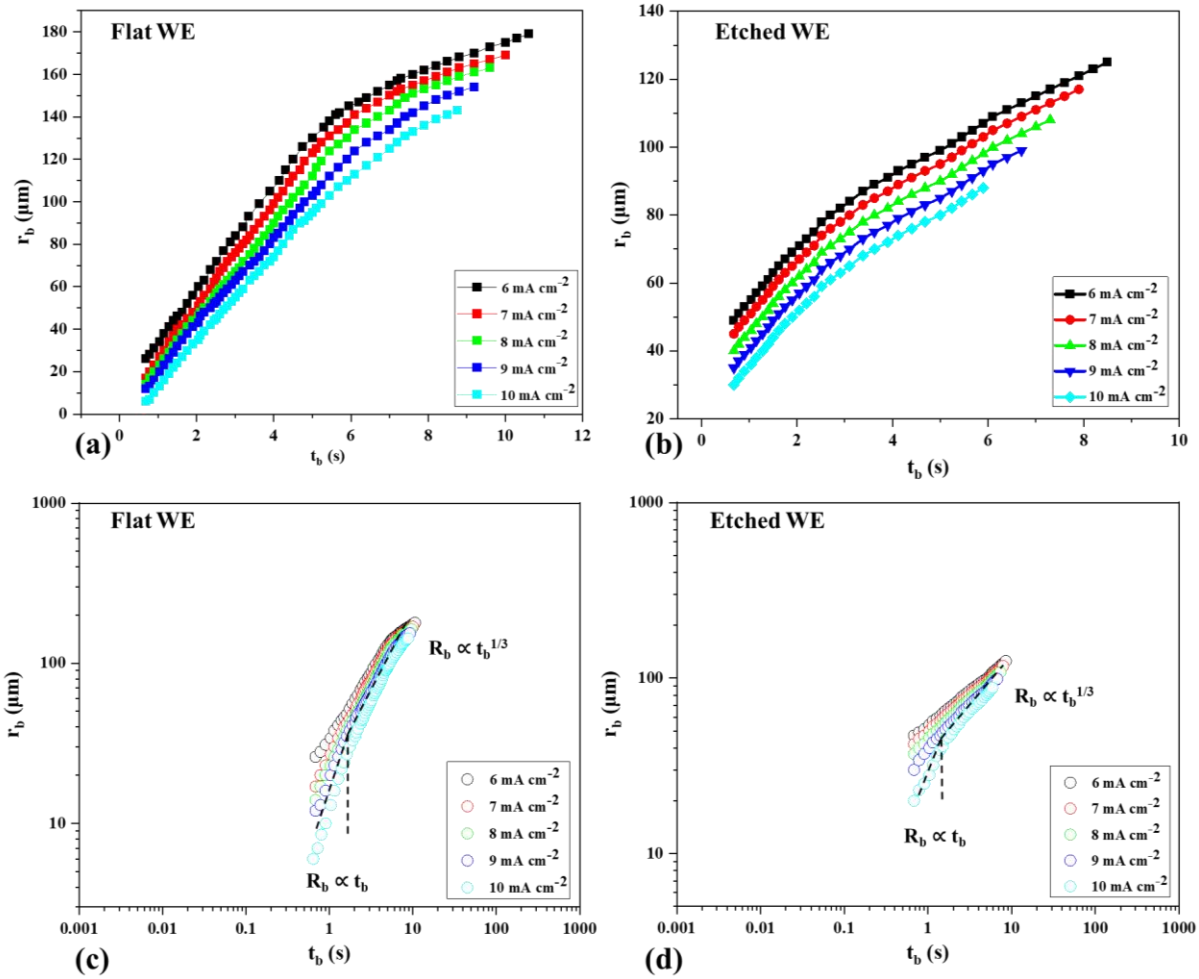

Figure 6. Bubble radius (r_b) vs. time (t_b) at various current densities using (a) Flat and (b) Etched WE. Logarithmic plot of the bubble radius (r_b) vs, time (t_b) at different current densities (6-10 mA cm^{-2}) using (c) Flat and (d) Etched WE

During electrolysis, the electrode potential fluctuates dynamically with the bubble evolution process [56]. As bubbles form and grow on the electrode surface, their expanding size reduces the active electrode area, leading to an increase in activation overpotential. When bubble coverage on the electrode surface reaches its maximum, the potential peaks at its highest voltage. Subsequently, the potential starts to decline as the active electrode area increases again, driven by bubbles detachment from the surface. Following detachment, new small bubbles rapidly nucleate, marking the beginning of the next growth cycle and continuing the sequence initiated by the previous bubble's detachment [57].

To analyse the H_2 evolution, chronopotentiometry measurements were conducted at 6 to 10 mA cm^{-2}. The fluctuation troughs in Figure 7 suggest the presence of bubbles on the WE. The peak voltage, labeled U_0, represents the baseline voltage required for electrochemical reaction at a specific current density, primarily determined by the applied current and electrolyte concentration. On the other hand, the valley voltage, marked as U_1, corresponds to the minimum voltage observed during a single gas evolution cycle. Both U_1 and U_0 stabilized about 20 s after the reaction began, indicating the formation of a stable concentration field with low further variation. The voltage fluctuation (ΔU) indicates the maximum overpotential induced by bubbles on the WE, defined as $\Delta U = U_1 - U_0$.

Figure 7(a, b) displays U-t plots obtained from experiments, revealing that ΔU exhibits similar shapes but varies in amplitude under different currents. To observe ΔU, the electrolysis process was first conducted for 20 s, followed by a 5 s recording period for both WEs. Results show that ΔU decreases at low current densities while increasing at high current

densities. This trend can be attributed to the limited availability of active sites at low current densities and their greater accessibility at higher current densities. Additionally, high current densities tend to enhance bubble formation and detachment, leading to more pronounced voltage fluctuations. These fluctuations arise from transient changes in electrode coverage and local ohmic resistance, further influencing the observed trends.

As depicted in Figure 7(a), using flat WE, ΔU is recorded as -0.004 V at 6 mA cm^{-2} and magnitude increased to -0.013 V, becoming more negative at 10 mA cm^{-2}. A similar trend is observed for the electrochemically etched WE but the amount of voltage for the same current densities is reduced due to the frequent bubbles detachment process. As shown in Figure 7(b), the ΔU using etched WE is -0.0018 V at 6 mA cm^{-2} and increased to -0.005 V at 10 mA cm^{-2}. The decrease in ΔU observed with the etched WE is likely attributed to the improved surface properties resulting from electrochemical etching. The optimized surface morphology of the etched WE significantly increased the electrochemically active surface area and promoted efficient bubble removal. These enhancements reduced overpotentials and stabilized the reaction dynamics, leading to the lowest voltage instability compared to the flat WE.

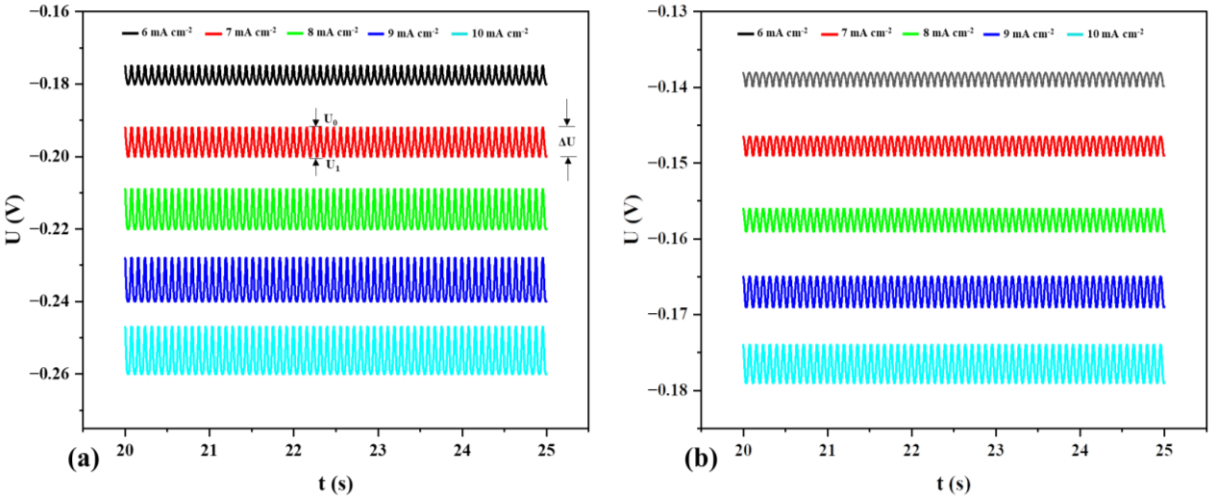

Figure 7. Voltage fluctuations induced by H_2 bubbles evolution at different current densities using (a) Flat and (b) Etched WE

3.3 Bubbles production efficiency

As shown in Figure 8(a), five bubbles with radii of 140, 125, 80, 60, and 40 µm are observed using both WEs. The active site with a critical bubble detachment radius of 140 µm produced 7 bubbles min^{-1}, while sites with r_b of 125, 80, 60, and 40 µm produced 9, 14, 19, and 27 bubbles min^{-1}, respectively. For the etched WE, bubbles with radii of 80, 60, 50, 40, and 30 µm are observed. It can be seen that the bubble production rate increased to 17, 23, 32, 47, and 88 bubbles min^{-1}. To compare the production rate of the same bubble critical radii, such as 80, 60, and 40 µm, the bubble production rate using etched WE represents a 21.42%, 21.05%, and 74.07% increase, respectively, compared to the flat WE. Figure 8(b) depicts the focused nucleation site with the bubble before and after detachment from the electrode surface having r_b of 140 µm.

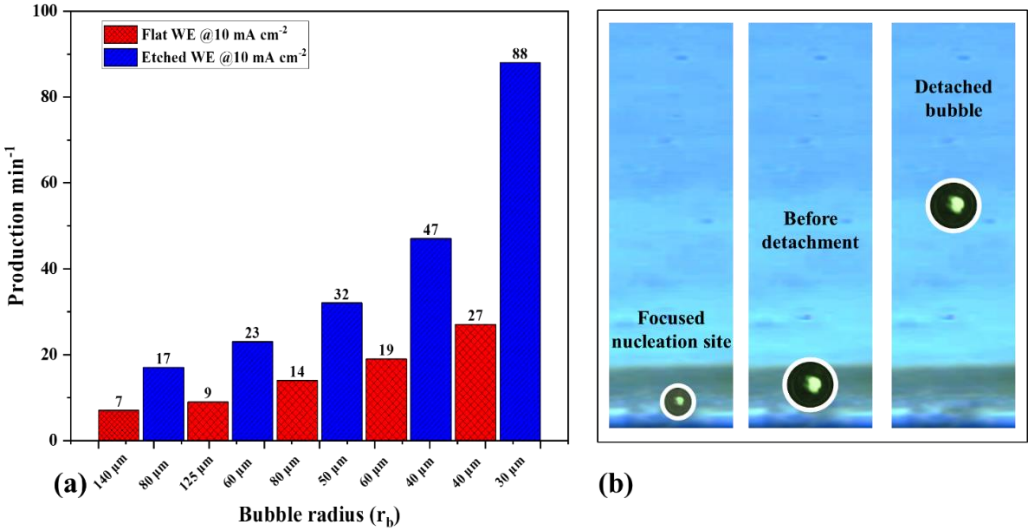

Figure 8. Bubbles production rate per minute from five different active sites at 10 mA cm^{-2} using (a) Flat and etched WE (b) Focused single nucleation site with bubble before and after detachment

The increased surface roughness of the etched WE minimizes the contact area between the bubbles and the electrode surface. This reduction in contact area weakens the adhesion forces that bind the bubbles to the electrode, enabling faster bubble detachment. As a result, active sites are cleared more efficiently, facilitating the next cycle of bubble formation and improving the overall dynamics of the electrolysis process [58]. The electrode roughness also disrupts the diffusion layer surrounding its surface, promoting better mass transport of reactants to the active sites. This enhanced movement of reactants improves the availability of ions and molecules necessary for the H_2 evolution reaction, thereby accelerating HER activity and contributing to higher efficiency in the electrolysis process [59]. Additionally, the rough surface prevents bubbles from merging, ensuring individual bubble production at multiple active sites. This is achieved through the presence of microchannels and surface asperities, which not only maintain bubble separation but also aid in their efficient detachment. This mechanism further optimizes the electrolysis process by minimizing blockages and enhancing continuous bubble release [60].

3.4 Nucleation Sites and Bubbles Distribution

This section examines the total number of nucleation sites and bubbles distribution on the WE at 10 mA cm^{-2} and –0.20 V vs. RHE. A high-speed camera, positioned perpendicular to the WE surface observes the nucleation sites and bubbles distribution. The electrolysis process was continuously carried out for three bubble growth-to-detachment cycles. For both WEs, the electrolysis process is initially run for 20 s, followed by a 10 s cut-off period. Subsequently, bubble activity is recorded for the next 30 s to ensure thorough observation of all nucleation sites and bubble distribution on the electrode surface.

As shown in Figure 9(a), the total number of nucleation sites within a 240 x 320 px focused area is 21 using the flat WE. The bubble radii were calculated using the same MATLAB algorithm applied consistently throughout the analysis. It is observed that the bubbles produced from the flat WE are generally larger compared to those generated from the etched WE. The bubble distribution in Figure 9(b) reveals that the majority of bubbles fall within the range of 100-180 µm, with an average bubble radius of 125.57 µm. This suggests that the flat WE tends to produce fewer but larger bubbles, which could be attributed to the uniformity of the surface and the limited availability of active nucleation sites. In contrast, the total number of nucleation sites significantly increases to 49 when using the etched WE, as illustrated in Figure 9(c). This increase in nucleation sites is likely due to the enhanced surface roughness and microstructural features introduced by the etching process, which provide more favorable locations for bubble formation. Consequently, the bubble size is notably reduced, with the majority of bubbles lying in the range of 80-120 µm, as depicted in Figure 9(d). The average bubble radius decreases to 95.55 µm, indicating that the etched WE promotes the formation of smaller, more numerous bubbles.

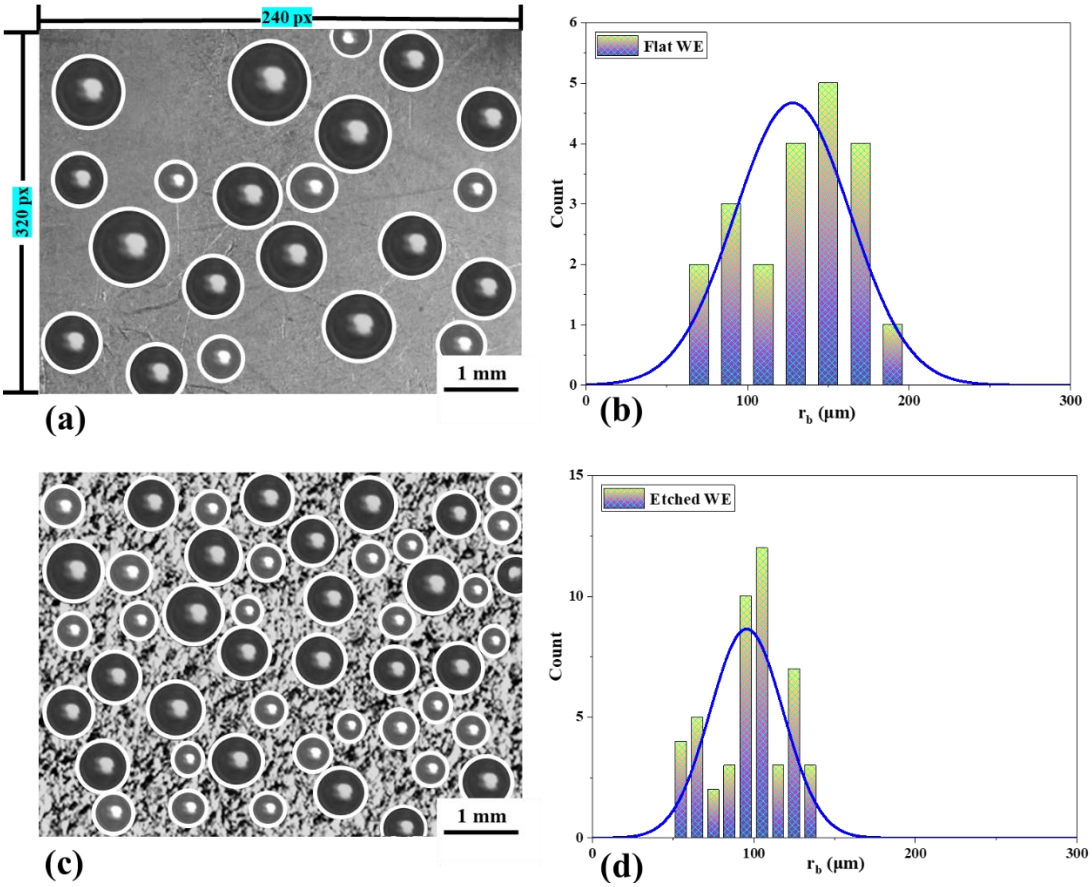

Figure 9. Shadowgraphy images show different bubbles with corresponding size distribution using (a, b) Flat and (c, d) Electrochemically etched Wes

The results demonstrate a clear trend of increasing bubble nucleation sites and a corresponding reduction in bubble size with increasing surface roughness. The maximum number of nucleation sites observed on the electrochemically etched WE is attributed to the enhanced surface area featuring a microporous structure. The micropores act as preferential sites for bubble nucleation, facilitating more frequent and localized gas evolution. The reduction in bubble size further underscores how progressively finer surface cavities promote bubble production. This phenomenon is likely due to the uniform and intricate microstructures created by etching, which generate numerous smaller cavities, limiting the space available for individual bubbles to expand.

Moreover, the smaller bubble size achieved with the etched WE minimizes the blockage of active sites by encouraging rapid bubbles detachment. This effect is critical in maintaining efficient electrochemical reactions, as it prevents the accumulation of bubbles that could otherwise hinder mass transport and reaction kinetics. The observed trend is consistent with previous studies, which have shown that rough electrodes with increased surface area tend to produce a higher density of smaller bubbles. These smaller bubbles exhibit reduced adhesion forces, enable faster detachment, enhance mass transport, higher current increase rate, and stabilize HER performance [61, 62].

3.5 HER Electrochemical Performance

The electrochemical performance of the WEs for the HER was evaluated using LSV and EIS in a 0.5 M KOH alkaline solution at a low scan rate of 2 mV s^{-1}. As depicted in Figure 10(a), the flat WE displayed lower HER activity than the electrochemically etched WE. The polarization curves revealed a gradual improvement in HER activity for etched WE. Specifically, the HER onset potential for the flat WE is 0.54 V and shifted to 0.43 V for the etched WE, representing a reduction of 0.11 V. The shift towards lower cathodic potential underscores the higher HER performance of the electrochemically etched WE.

To further assess the electrocatalytic efficiency, the overpotential (η_{10}) was measured at a current density of 10 mA cm^{-2}. As illustrated in Figure 10(b), the overpotential for the flat WE is 331.4 mV, while the etched WE exhibited a notably lower overpotential of 247.8 mV. Additionally, at a higher current density of 50 mA cm^{-2}, the etched WE demonstrated an overpotential (η_{50}) of 328.4 mV. The enhanced HER activity of the etched WE can be primarily attributed to its increased surface area with micropores, which provides a maximum number of active sites for H_2 evolution. In contrast, the flat WE experienced slower H_2 bubble detachment, leading to prolonged bubble accumulation on its surface. This accumulation increased the overpotential required for the electrochemical reaction, as the trapped bubbles blocked active sites and impeded ionic conductivity. On the other hand, the optimized surface morphology of the etched WE facilitated faster bubble detachment, effectively reducing bubble-induced resistance and lowering the overpotential.

The HER mechanism was further examined using the Tafel slope. Tafel plots were generated from LSV curves following the Tafel equation $\eta = a + b \log j$, where η denotes overpotential, a is the Tafel intercept, b represents the Tafel slope, and j is the current density [63]. The overall H_2 reduction reaction under alkaline conditions ($2H_2O + 2e^- \rightarrow H_2 + 2OH^-$) proceeds through the following three reaction steps (R1-R3), that describe the mechanistic pathway of alkaline HER:

$$\text{Volmer reaction: } H_2O + e^- \rightarrow H^* + OH^- \quad (R1)$$

$$\text{Heyrovsky reaction: } H_2O + e^- + H^* \rightarrow H_2 + OH^- \quad (R2)$$

$$\text{Tafel reaction: } H^* + H^* \rightarrow H_2 \quad (R3)$$

A Tafel slope of 30 mV dec^{-1} signifies that the Tafel reaction is the rate-determining step, while slopes of 40 and 120 mV dec^{-1} correspond to the Heyrovsky and Volmer reaction steps being rate-determining, respectively. Lower Tafel slopes are advantageous, as they reflect enhanced HER kinetics [64]. The Tafel slope using Flat WE is 154.3 mV dec^{-1} and decreased to 132.7 mV dec^{-1} using etched WE as depicted in Figure 10(c). The observed slope of approximately 132.7 mV dec^{-1} suggests that the hydrogen evolution reaction is predominantly governed by the Volmer–Heyrovsky mechanism, where the initial discharge of protons onto the electrode surface (Volmer step) is followed by an electrochemical desorption step (Heyrovsky step). The slope being slightly higher than the ideal 120 mV dec^{-1} implies that the Volmer step remains the rate-limiting process, but the subsequent Heyrovsky reaction also contributes significantly to the overall kinetics. Similar findings have been reported in recent studies on surface-modified stainless steel electrodes, where electrochemical etching or nanoporous activation enhanced HER activity and shifted the rate-determining step toward the Volmer–Heyrovsky pathway [65]. The reduction in the Tafel slope for the etched WE can be ascribed to the increased surface area induced by the electrochemical etching process, which facilitates more efficient electron transfer and improved catalytic activity. Table 1 presents the comparison of HER performance using electrochemically etched WE with different surface-modified SS electrodes.

Electrochemical impedance spectroscopy is a crucial technique for evaluating the charge transfer rate at the electrode-electrolyte interface during HER process [66]. As shown in Figure 10(d), EIS analysis of both flat and electrochemically etched WEs reveals that the etched WE exhibits the smallest semi-arc, indicating superior charge transfer kinetics. Equivalent circuit simulations yield a charge transfer resistance (R_{ct}) of 67.2 Ω for the etched WE, significantly lower than the 234.3 Ω observed for the flat WE. These findings underline that the etched WE demonstrates faster HER kinetics, which aligns with HER activity trends seen in Figure 10(a-c).

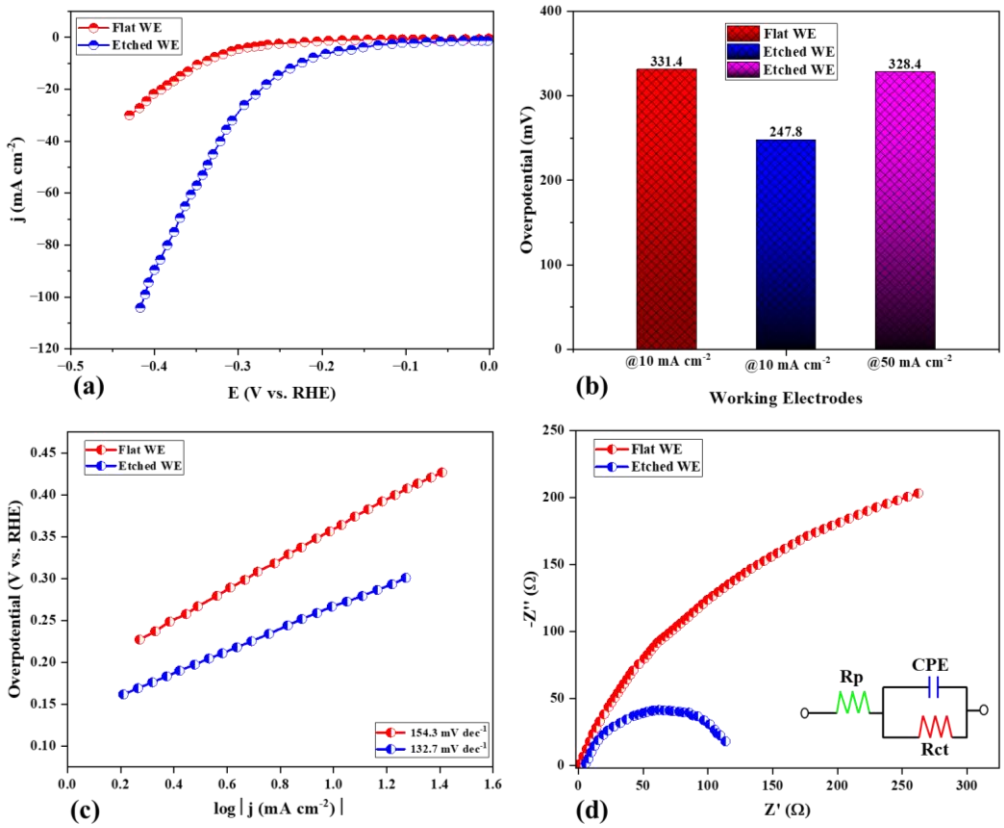

Figure 10. (a) HER LSV curves for both WEs (b) Corresponding overpotential at 10 and 50 mA cm^{-2} (c) Tafel slopes derived from LSV curves, and (d) EIS plots with the equivalent circuit model

Table 1. Comparison of the HER activity of electrochemically etched WE with reported literature

Electrodes	η_{10} (mV)	η_{50} (mV)	Tafel slope (mV dec^{-1})	Ref
Etched SS-316L WE	247.8	328.4	132.7	This work
SS-100 316L	344.0	---	136.6	[67]
SS-500 316L	318.2	425.6	126.5	
SS-1000 316L	289.8	380.5	120.1	
SS-1600 316L	209.8	314.7	115.6	
SS-2000 316L	269.1	359.3	126.1	
SS-2800 316L	238.2	334.5	118.4	
SS-1600 304	255.4	374.9	120.9	
AISI-302	438.0	---	151.0	[68]
AISI-304	432.0	---	143.0	
AISI-316	424.0	---	158.0	
AISI-321	442.0	---	159.0	
SSM	462.0	588.0	110.0	[69]
CoP	264.0	348.0	105.0	
1Ni@CoP	240.0	349.0	109.0	
5Ni@CoP	205.0	320.0	82.0	
10Ni@CoP	181.0	282.0	69.0	
SS mesh-1600	330.0	---	147.0	[70]
MoS_2/SS-500	208.0	257.0	145.0	
MoS_2/SS-2000	189.0	229.0	130.0	
MoS_2/CC	196.0	240.0	82.0	
SS-304	370.0	---	---	[71]
ESS	466.0	---	---	

To further evaluate the ECSA of the WEs, the slopes obtained from CV measurements and linear fitting were used to calculate Cdl, which enabled estimation of the ECSA for both WEs [72]. As depicted in Figure 11(a), CV tests for both WEs were performed at 0.10–0.20 V vs. RHE, at scan rates of 5, 10, 20, and 30 mV s^{-1}. Figure 11(b) shows the capacitance current plots at 0.15 V (vs. RHE) against scan rates, where the linear fitting slope was effectively used to estimate Cdl [73]. As a result, the Cdl of the etched WE is 0.91 mF cm^{-2}, significantly higher than the Flat WE (0.38 mF cm^{-2}). The increased Cdl value indicates that the electrochemically etched WE possesses a larger ECSA, leading to improved conductivity and enhanced electron transport characteristics, which align with its superior HER performance.

The stability test plays a critical role in evaluating the long-term performance of electrodes [74]. In this study, as shown in Figure 11(c), the stability of the etched WE was examined by comparing the LSV curves before and after 500 CV cycles at 100 mV s^{-1}. Notably, after 500 cycles, the polarization curves exhibit minimal variation, indicating good stability during long-term operation. Moreover, the presence of micropores on the electrode surface mitigates localized degradation, ensuring sustained performance over time [75]. The superior conductivity and efficient charge transfer properties of the electrochemically etched WE further enhance its stability during prolonged HER operations. The good stability, combined with the industrial scalability and cost-effectiveness, underscores the significant potential of the electrochemically etched WEs for practical H_2 production applications.

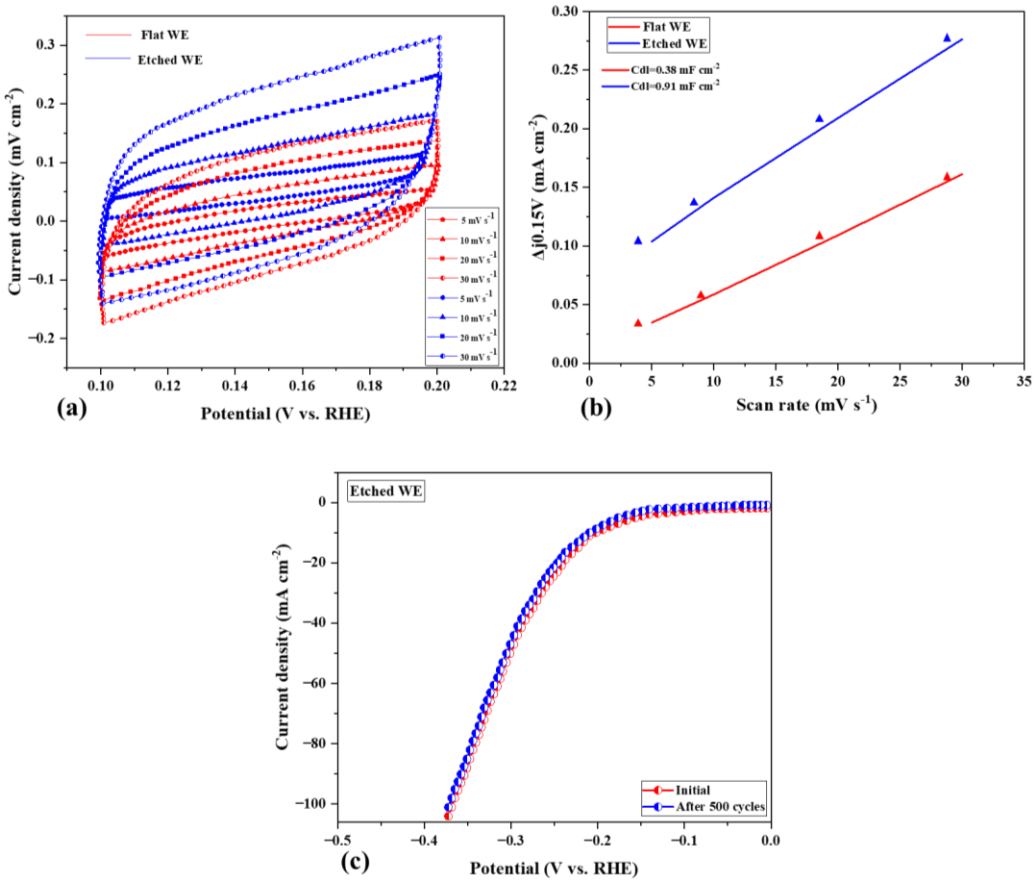

Figure 11. CV measurements with different scan rates ranging from 0.10-0.20 V vs. RHE for (a) Flat and etched WE. (b) Estimation of the ECSA from Cdl versus scan rate at 0.15 V vs. RHE (Δj=0.15 V). (c) Stability test of the etched WE after 500 CV cycles

4. CONCLUSIONS

This study explored how surface roughness influences hydrogen bubble dynamics and electrochemical performance using flat and electrochemically etched SS-316L WEs. The results revealed a significant impact of surface roughness on various parameters, including bubble size, growth time, voltage fluctuations, bubble production efficiency, velocity, distribution, and HER performance in a 0.5 M KOH solution. The key findings are summarized as follows:

i) Hydrogen Bubble Dynamics:

It is observed that the increase in current density (6-10 mA cm^{-2}) significantly reduces bubble detachment radii and lifetime for both WEs, with electrochemically etched WE showing progressively smaller detachment radii than flat surface. The growth patterns of H_2 bubbles are similar across both WEs, suggesting that surface roughness does not directly impact bubble growth. However, higher surface roughness and current density contribute to enhanced bubble detachment and shorter bubble lifetimes. Chronopotentiometry reveals similar voltage fluctuation trends across electrodes, with magnitudes decreasing for the etched WE due to enhanced bubble detachment. It is found that using Flat

WE, the ΔU is –0.004 V at 6 mA cm^{-2} and increases to –0.013 V, becoming more negative at 10 mA cm^{-2}. The ΔU using etched WE is -0.0018 V at 6 mA cm^{-2} and increased to -0.005 V at 10 mA cm^{-2}, indicating the best performance, as its optimized surface morphology provided superior wettability, reduced overpotentials, and stabilized reaction dynamics, resulting in the lowest voltage instability compared to the Flat WE.

ii) Bubbles production efficiency, Nucleation sites, and Bubble distribution:

Bubble production efficiency increases with surface roughness. The etched WE exhibited the maximum bubble production rate (88 bubbles min^{-1} for 30 µm radius) compared to the flat WE (27 bubbles min^{-1} for 40 µm radius). In contrast, bubble velocity is highest for the flat WE due to larger bubble size but reduces for the etched WE due to smaller bubble radii. The increase in the number of nucleation sites and a corresponding reduction in bubble size is observed with increasing surface roughness. The flat WE produced fewer nucleation sites and larger bubbles (150-180 µm), while etched WE showed an increase in the nucleation sites.

iii) Electrochemical Performance and Stability:

Among both WEs, the electrochemically etched WE exhibited superior HER activity, with an onset potential of 0.43 V, a reduction of 0.11 V compared to the flat WE (0.54 V). At 10 mA cm^{-2}, the overpotential decreases from 331.4 mV (flat WE) to 247.8 mV (etched WE). Electrochemical impedance spectroscopy reveals the smallest charge transfer resistance for the etched WE (67.2 Ω) compared to 234.3 Ω for the flat WE. The double-layer capacitance of etched WE is 0.91 mF cm^{-2}, significantly higher than flat WE (0.38 mF cm^{-2}), indicating a larger electrochemically active surface area, consistent with its higher HER performance. The etched WE exhibits excellent stability, showing slight variation in polarization curves after 500 CV cycles at a scan rate of 100 mV s^{-1}.

ACKNOWLEDGEMENTS

The authors gratefully acknowledge the support given by the Universiti Teknologi Petronas to the Center of Sustainable Resources for Intelligent and Efficient Mobility (CSRIEM), in performing this research through the internal grant OPEX, Malaysia, with grant number (015LB0-101).

FUNDING

This study was not supported by any grants from funding bodies in the public, private, or not-for-profit sectors.

CONFLICT OF INTEREST

The authors declare no conflicts of interest.

AUTHORS' CONTRIBUTION

W.U. Mulk (Investigation; Writing - original draft; Methodology; Conceptualization)

A.R.A. Aziz (Supervision)

A.A. Ghoto (Visualization; Formal analysis)

R. Khatoon (Formal analysis)

M.A. Ismael (Investigation; Writing - review & editing; Conceptualization)

M.A. Said (Formal analysis)

AVAILABILITY OF DATA AND MATERIALS

The datasets generated during and/or analyzed during the current study are available from the corresponding author on reasonable request.

ETHICS STATEMENT

This study does not involve human participants or animal subjects. No ethics approval is required.

REFERENCES

[1] W. U. Mulk, S. A. Ali, S. N. Shah, M. U. H. Shah, Q. J. Zhang, M. Younas, et al., "Breaking boundaries in CO_2 capture: Ionic liquid-based membrane separation for post-combustion applications," *Journal of CO_2 Utilization*, vol. 75, p. 102555, 2023.

[2] M. A. Ismael, I. R. Silmyi, W. U. Mulk, M. El-Adawy, A. R. A. Aziz, M. E. Babiker, "The role of nanoparticles in combustion improvement: Performance and emission analysis of a DI diesel engine fuelled with water-in-biodiesel emulsions enhanced by mono and hybrid nanoparticles," *Applied Thermal Engineering*, vol. 274, p. 126755, 2025.

[3] W. U. Mulk, M. A. Ismael, A. R. A. Aziz, M. Azman, M. Aider, M. Younas, et al., "Recent progress in biodiesel-fueled ICEs and role of nano-additives in optimizing combustion and emissions with cost analysis: A comprehensive review," *Renewable and Sustainable Energy Reviews*, vol. 226, p. 116263, 2026.

[4] C. McGregor, B. D. Young, and D. Hildebrandt, "Risk assessment framework for green hydrogen megaprojects: Balancing climate goals with project viability," *Applied Thermal Engineering*, vol. 262, P. 125197, 2025.

[5] M. A. Ismael, C. S. Maung, A. R. A. Aziz, W. U. Mulk, W. B. Ayandotun, I. Veza, et al., "Ammonia as a hydrogen carrier in dual-fuel diesel engines: Influence of ammonia and oxygen on combustion performance and emissions," *International Journal of Hydrogen Energy*, vol. 165, p. 150586, 2025.

[6] Y. Wang, B. Su, X. Yang, Z. Chen, and S. Wang, "A green hydrogen production system based on solar-assisted biogas steam reforming," *Applied Thermal Engineering*, vol. 248, p. 123067, 2024.

[7] W. U. Mulk, A. R. Abd Aziz, M. A. Ismael, and A. A. Ghoto, "Diesel and oxyhydrogen dual-fuel: Reducing emissions of a diesel engine using diesel–oxyhydrogen dual-fuel combustion," *Journal of Advanced Research in Experimental Fluid Mechanics and Heat Transfer*, vol. 18, no. 1, pp. 69–80, 2025.

[8] E. M. A. Mokheimer, M. R. Shakeel, A. Harale, S. Paglieri, and R. B. Mansour, "Fuel reforming processes for hydrogen production," *Fuel*, vol. 359, p. 130427, 2024.

[9] L. Jin, R. N. Nakashima, G. Comodi, H. L. Frandsen, "Alkaline electrolysis for green hydrogen production: A novel, simple model for thermo-electrochemical coupled system analysis," *Applied Thermal Engineering*, vol. 262, p. 125154, 2025.

[10] W. U. Mulk, A. R. A. Aziz, M. A. Ismael, A. A. Ghoto, S. A. Ali, M. Younas, et al., "Electrochemical hydrogen production through anion exchange membrane water electrolysis (AEMWE): Recent progress and associated challenges in hydrogen production," *International Journal of Hydrogen Energy*, vol. 94, pp. 1174–1211, 2024.

[11] W. Zhang, Y. Chen, Z. Ma, Z. Sun, J. Wang, J. Feng. et al., "Challenges and strategies of transition metal phosphides applied in oxygen evolution reaction of electrocatalytic water splitting: A review," *Fuel*, vol. 369, p. 131741, 2024.

[12] J. Zhu, X. Zhang, P. Lv, Y. Wang, and J. Wang, "An experimental investigation of convective mass transfer characterization in two configurations of electrolysers," *International Journal of Hydrogen Energy*, vol. 43, no. 18, pp. 8632–8643, 2018.

[13] Y.-H. Li and Y.-J. Chen, "The effect of magnetic field on the dynamics of gas bubbles in water electrolysis," *Scientific Reports*, vol. 11, no. 1, P. 9346, 2021.

[14] K. M. Cho, P. R. Deshmukh, and W. G. Shin, "Hydrodynamic behavior of bubbles at gas-evolving electrode in ultrasonic field during water electrolysis," *Ultrasonics Sonochemistry*, vol. 80, P. 105796, 2021.

[15] Y. Yu, Y. Zhong, M. Wang, and Z. Guo, "Electrochemical behavior of aluminium anode in super-gravity field and its application in copper removal from wastewater by electrocoagulation," *Chemosphere*, vol. 272, P. 129614, 2021.

[16] K. Khowamnuaychok, C. Luangchaisri, and C. Muangphat, "Effect of surface curvature and wettability on the shape of nanobubble and hollow structure of gold nanoparticles," *Surfaces and Interfaces*, vol. 60, P. 106045, 2025.

[17] J. Shen, J. Li, B. Li, Y. Zheng, X. Bao, J. Guo, et al., "Ambient fast synthesis of superaerophobic/superhydrophilic electrode for superior electrocatalytic water oxidation," *Energy & Environmental Materials*, vol. 6, no. 6, p. e12462, 2023.

[18] X. Qin, B. Yan, D. Kim, Z. Teng, T. Chen, J. Choi, et al., "Interfacial engineering and hydrophilic/aerophobic tuning of Sn_4P_3/Co_2P heterojunction nanoarrays for high-efficiency fully reversible water electrolysis," *Applied Catalysis B: Environmental*, vol. 304, p. 120923, 2022.

[19] S. Chang, Y. Zhang, B. Zhang, X. Cao, L. Zhang, X. Huang, et al., "Conductivity modulation of 3D-printed shellular electrodes through embedding nanocrystalline intermetallics into amorphous matrix for ultrahigh-current oxygen evolution," *Advanced Energy Materials*, vol. 11, no. 28, p. 2100968, 2021.

[20] K. Ge, Y. Zeng, G. Dong, L. Zhao, Z. Wang, and M. Huang, "3D self-standing grass-like cobalt phosphide vesicles-decorated nanocones grown on Ni-foam as an efficient electrocatalyst for hydrogen evolution reaction," *International Journal of Hydrogen Energy*, vol. 44, no. 26, pp. 13490–13501, 2019.

[21] E. Hatami, A. Toghraei, and G. Barati Darband, "Electrodeposition of Ni–Fe micro/nano urchin-like structure as an efficient electrocatalyst for overall water splitting," *International Journal of Hydrogen Energy*, vol. 46, no. 14, pp. 9394–9405, 2021.

[22] Y. Li, H. Zhang, T. Xu, Z. Lu, X. Wu, P. Wan, et al., "Under-water superaerophobic pine-shaped Pt nanoarray electrode for ultrahigh-performance hydrogen evolution," *Advanced Functional Materials*, vol. 25, no. 11, pp. 1737–1744, 2015.

[23] D. Kim, X. Qin, B. Yan, Y. Piao, "Sprout-shaped Mo-doped CoP with maximized hydrophilicity and gas bubble release for high-performance water splitting catalyst," *Chemical Engineering Journal*, vol. 408, p. 127331, 2021.

[24] X. Wang, X. Xia, H. Wang, Y. Yang, S. Yang, A. Zhang, et al., "Special-wettability-mediating electrode interfaces for new energy devices: Opportunities and challenges," *Nano Energy*, vol. 120, p. 109185, 2024.

[25] Y. Yu, P. Liu, M. Dou, J. Niu, Z. Zhang, F. Wang, "Promotion of hydrogen evolution catalysis by ordered hierarchically porous electrodes," *Catalysis Science & Technology*, vol. 11, no. 9, pp. 2997–3001, 2021.

[26] F. Wang, Y. Wu, B. Dong, K. Lv, Y. Shi, N. Ke, et al., "Robust porous WC-based self-supported ceramic electrodes for high current density hydrogen evolution reaction," *Advanced Science*, vol. 9, no. 15, p. 2106029, 2022.

[27] W. Song, M. Xu, X. Teng, Y. Niu, S. Gong, X. Liu, et al., "Construction of self-supporting, hierarchically structured caterpillar-like $NiCo_2S_4$ arrays as an efficient trifunctional electrocatalyst for water and urea electrolysis," *Nanoscale*, vol. 13, no. 3, pp. 1680–1688, 2021.

[28] A. Z. Alhakemy, A. B. A. A. Nassr, A. E.-H. Kashyout, Z. Wen, "Modifying the 316L stainless steel surface by an electrodeposition technique: Towards high-performance electrodes for alkaline water electrolysis," *Sustainable Energy & Fuels*, vol. 6, no. 5, pp. 1382–1397, 2022.

[29] U. K. Sultana, J. F. S. Fernando, A. P. O'Mullane, "Transformation of stainless steel 316 into a bifunctional water splitting electrocatalyst tolerant to polarity switching," *Sustainable Materials and Technologies*, vol. 25, P. e00177, 2020.

[30] M. J. Lavorante, J. I. Franco, "Performance of stainless steel 316L electrodes with modified surface to be use in alkaline water electrolyzers," *International Journal of Hydrogen Energy*, vol. 41, no. 23, pp. 9731–9737, 2016.

[31] K. Zeng, D. Zhang, "Evaluating the effect of surface modifications on Ni based electrodes for alkaline water electrolysis," *Fuel*, vol. 116, pp. 692–698, 2014.

[32] T. Zhou, H. Gao, Y. Hu, W. Huang, F. Yang, W. Sun, et al., "Activation stainless steel with electrochemical etching-hydrothermal as an efficient and stable alkaline water oxidation electrode," *Journal of Power Sources*, vol. 577, p. 233241, 2023.

[33] H. Y. Cai, J. F. Ma, N. N. Li, W. P. Li, S. P. Li, M. X. Qiu, et al., "Investigation on hydrogen evolution reaction performance of porous electrode prepared by laser powder bed fusion," *Renewable Energy*, vol. 185, pp. 771–778, 2022.

[34] X. Lyu, J. Li, C. J. Jafta, Y. Bai, C. P. Canales, F. Magnus, et al., "Investigation of oxygen evolution reaction with Ni foam and stainless-steel mesh electrodes in alkaline seawater electrolysis," *Journal of Environmental Chemical Engineering*, vol. 10, no. 5, p. 108486, 2022.

[35] C. Lee, A. Kim, J. Kim, "Electrochemically etched porous stainless steel for enhanced oil retention," *Surface and Coatings Technology*, vol. 264, pp. 127–131, 2015.

[36] A. Dehane, S. Merouani, O. Hamdaoui, A. Alghyamah, "A complete analysis of the effects of transfer phenomena and reaction heats on sono-hydrogen production from reacting bubbles: Impact of ambient bubble size," *International Journal of Hydrogen Energy*, vol. 46, no. 36, pp. 18767–18779, 2021.

[37] Y. Kameya, R. Hasegawa, and T. Osawa, "Hydrogen bubble management in planarly confined aqueous electrolyte: Fundamental factors for scale-up reactor design," *International Journal of Hydrogen Energy*, vol. 139, pp. 963–970**,** 2025.

[38] A. Raman, P. Peñas, D. van der Meer, D. Lohse, H. Gardeniers, D. Fernández Rivas, "Potential response of single successive constant-current-driven electrolytic hydrogen bubbles spatially separated from the electrode," *Electrochimica Acta*, vol. 425, p. 140691, 2022.

[39] P. van der Linde, A Moreno Soto, P Peñas-López, J. R.-Rodríguez, D. Lohse, H. Gardeniers, et al., "Electrolysis-driven and pressure-controlled diffusive growth of successive bubbles on microstructured surfaces," *Langmuir*, vol. 33, no. 45, pp. 12873–12886, 2017.

[40] A. Raman, C. C. dos Santos Porto, H. Gardeniers, C. Soares, D. F. Rivas, N. Padoin, "Investigating mass transfer around spatially-decoupled electrolytic bubbles," *Chemical Engineering Journal*, vol. 477, p. 147012, 2023.

[41] D. Fernández, P. Maurer, M. Martine, J. M. D. Coey, and M. E. Möbius, "Bubble formation at a gas-evolving microelectrode," *Langmuir*, vol. 30, no. 43, pp. 13065–13074, 2014.

[42] Y. Wang, M. E. Zaytsev, H. L. The, J. C. T. Eijkel, H. J. W. Zandvliet, X. Zhang, et al., "Vapor and gas-bubble growth dynamics around laser-irradiated, water-immersed plasmonic nanoparticles," *ACS Nano*, vol. 11, no. 2, pp. 2045–2051, 2017.

[43] F. Liu, F. Wang, X. Hao, Z. Fan, J. Tan, "Effects of foam cathode electrode structure on alkaline water electrolysis for hydrogen production," *Chemical Engineering Science*, vol. 298, p. 120307, 2024.

[44] S. Wang, K. Liu, X. Yao, L. Jiang, "Bioinspired surfaces with superwettability: New insight on theory, design, and applications," *Chemical Reviews*, vol. 115, no. 16, pp. 8230–8293, 2015.

[45] G.-H. Ban, Y. Li, M. M. Wall, and S. Jun, "A nanoengineered stainless steel surface to combat bacterial attachment and biofilm formation," *Foods*, vol. 9, no. 11, p. 1518, 2020.

[46] C. Zhu, D. Du, A. Eychmüller, Y. Lin, "Engineering ordered and nonordered porous noble metal nanostructures: Synthesis, assembly, and their applications in electrochemistry," *Chemical Reviews*, vol. 115, no. 16, pp. 8896–8943, 2015.

[47] Y. He, S. Liu, M. Wang, Q. Cheng, T. Qian, C. Yan, "Deciphering engineering principle of three-phase interface for advanced gas-involved electrochemical reactions," *Journal of Energy Chemistry*, vol. 80, pp. 302–323, 2023.

[48] H. Imanzadeh, A. Khataee, M. Nozari-Asbemarz, J. J. Leahy, M. Amiri, "A facile strategy for synthesis of flower-like $FeNiS_2$ nanocomposite via integration of binary metal-organic framework and metal sulfide for enhanced electrocatalytic oxygen evolution reaction," *Surfaces and Interfaces*, vol. 53, p. 105049, 2024.

[49] X. Lu, D. Yadav, L. Zhou, X. Li, L. Ma, D. Jing, "Evolution of hydrogen bubbles on a microelectrode driven by constant currents and its impact on potential response," *Chemical Engineering Journal*, vol. 500, p. 156890, 2024.

[50] J. Park, M. J. Kim, Y. Kim, S. Lee, S. Park, W. Yang, "Insights into bubble dynamics in water splitting," *ACS Energy Letters*, vol. 10, no. 1, pp. 212–237, 2025.

[51] J. Görtz, J. Seiler, P. Kolmer, A. Jupke, "Raising the curtain: Bubble size measurement inside parallel plate electrolyzers," *Chemical Engineering Science*, vol. 286, p. 119550, 2024.

[52] P. Chandran, S. Bakshi, D. Chatterjee, "Study on the characteristics of hydrogen bubble formation and its transport during electrolysis of water," *Chemical Engineering Science*, vol. 138, pp. 99–109, 2015.

[53] Y. He, Y. Cui, Z. Zhao, Y. Chen, W. Shang, P. Tan, "Strategies for bubble removal in electrochemical systems," *Energy Reviews*, vol. 2, no. 1, p. 100015, 2023.

[54] J. Qin, T. Xie, D. Zhou, L. Luo, Z. Zhang, Z. Shang, et al., "Kinetic study of electrochemically produced hydrogen bubbles on Pt electrodes with tailored geometries," *Nano Research*, vol. 14, no. 7, pp. 2154–2159, 2021.

[55] N. Bidin, S. R. Azni, M. A. A. Bakar, A. R. Johari, D. H. F. A. Munap, M. F. Salebi, et al., "The effect of sunlight in hydrogen production from water electrolysis," *International Journal of Hydrogen Energy*, vol. 42, no. 1, pp. 133–142, 2017.

[56] X. Zhao, H. Ren, L. Luo, "Gas bubbles in electrochemical gas evolution reactions," *Langmuir*, vol. 35, no. 16, pp. 5392–5408, 2019.

[57] X. Liu, S. Zheng, K. Wang, "Influence of bubble generation on the microchannel electrochemical gas evolution reaction," *Chemical Engineering Journal*, vol. 463, p. 142453, 2023.

[58] J. Du, B. Liu, Y. Zhao, "Nucleation bubble boundary layer theory for ultra-fast electrochemical polishing of additive manufacturing components," *Additive Manufacturing*, vol. 92, p. 104362, 2024.

[59] M. Aghasibeig, C. Moreau, A. Dolatabadi, R. Wuthrich, "Fabrication of nickel electrode coatings by combination of atmospheric and suspension plasma spray processes," *Surface and Coatings Technology*, vol. 285, pp. 68–76, 2016.

[60] B. J. Plowman, L. A. Jones, S. K. Bhargava, "Building with bubbles: The formation of high surface area honeycomb-like films via hydrogen bubble templated electrodeposition," *Chemical Communications*, vol. 51, no. 21, pp. 4331–4346, 2015.

[61] M. Li, P. Xie, L. Yu, L. Luo, X. Sun, "Bubble engineering on micro-/nanostructured electrodes for water splitting," *ACS Nano*, vol. 17, no. 23, pp. 23299–23316, 2023.

[62] G. Tang, Y. Chen, J. Chen, L. Liu, H. Wen, W. Liu, et al., "Flow-through porous electrode for enhanced oxygen evolution reaction by promoting gas bubble release from water splitting," *Chemical Engineering Science*, vol. 296, p. 120242, 2024.

[63] P. Xiao, Y. Yan, X. Ge, Z. Liu, J.-Y. Wang, X. Wang, "Investigation of molybdenum carbide nano-rod as an efficient and durable electrocatalyst for hydrogen evolution in acidic and alkaline media," *Applied Catalysis B: Environmental*, vol. 154–155, pp. 232–237, 2014.

[64] Y.-R. Liu, X. Li, G. Q. Han, B. Dong, W. H. Hu, X. Shang, et al., "Template-assisted synthesis of highly dispersed MoS_2 nanosheets with enhanced activity for hydrogen evolution reaction," *International Journal of Hydrogen Energy*, vol. 42, no. 4, pp. 2054–2060, 2017.

[65] Y. Lyu, R. Wang, L. Tao, Y. Zou, H. Zhou, T. Liu, et al., "In-situ evolution of active layers on commercial stainless steel for stable water splitting," *Applied Catalysis B: Environmental*, vol. 248, pp. 277–285, 2019.

[66] S. Jing, L. Zhang, L. Luo, J. Lu, S. Yin, P. K. Shen, et al., "N-doped porous molybdenum carbide nanobelts as efficient catalysts for hydrogen evolution reaction," *Applied Catalysis B: Environmental*, vol. 224, pp. 533–540, 2018.

[67] Y. Liu, K. Zhang, D. Zhang, W. Dong, T. Jiang, H. Zhou, et al., "Industrial stainless steel meshes for efficient electrocatalytic hydrogen evolution," *Journal of Energy Storage*, vol. 41, p. 102844, 2021.

[68] I. Barauskienė, G. Laukaitis, E. Valatka, "Stainless steel as an electrocatalyst for overall water splitting under alkaline and neutral conditions," *Journal of Electroanalytical Chemistry*, vol. 950, p. 117880, 2023.

[69] A. A. M. Abahussain, A. F. Alharbi, W. Wazeer, H. El-Deeb, A. B. A. A. Nassr, "Stainless steel as gas evolving electrodes in water electrolysis: Boosting the electrocatalytic hydrogen evolution reaction on electrodeposited Ni@CoP modified stainless steel electrodes," *Fuel*, vol. 368, p. 131605, 2024.

[70] K. Zhang, Y. Liu, B. Wang, F. Yu, Y. Yang, L. Xing, et al., "Three-dimensional interconnected MoS_2 nanosheets on industrial 316L stainless steel mesh as an efficient hydrogen evolution electrode," *International Journal of Hydrogen Energy*, vol. 44, no. 3, pp. 1555–1564, 2019.

[71] M. Kim, J. Ha, N. Shin, Y.-T. Kim, J. Choi, "Self-activated anodic nanoporous stainless steel electrocatalysts with high durability for the hydrogen evolution reaction," *Electrochimica Acta*, vol. 364, p. 137315, 2020.

[72] T. Feng, Q Zeng, S Lu, M Yang, S Tao, Y. Chen, Y. Zhou, et al., "Morphological and interfacial engineering of cobalt-based electrocatalysts by carbon dots for enhanced water splitting," *ACS Sustainable Chemistry & Engineering*, vol. 7, no. 7, pp. 7047–7057, 2019.

[73] B. Mao, B. Wang, F. Yu, K. Zhang, Z. Zhang, J. Hao, et al., "Hierarchical MoS_2 nanoflowers on carbon cloth as an efficient cathode electrode for hydrogen evolution under all pH values," *International Journal of Hydrogen Energy*, vol. 43, no. 24, pp. 11038–11046, 2018.

[74] W. Dong, H. Zhou, B. Mao, Z. Zhang, Y. Liu, Y. Liu, et al., "Efficient MOF-derived V–Ni_3S_2 nanosheet arrays for electrocatalytic overall water splitting in alkali," *International Journal of Hydrogen Energy*, vol. 46, no. 18, pp. 10773–10782, 2021.

[75] M. Pierpaoli, P. Jakobczyk, and M. Sawczak, et al., "Carbon nanoarchitectures as high-performance electrodes for the electrochemical oxidation of landfill leachate," *Journal of Hazardous Materials*, vol. 401, p. 123407, 2021.

NOMENCLATURE

Acronyms	
AFM	Atomic force microscopy
Ag/AgCl	Silver on silver chloride
AWE	Alkaline water electrolysis
CE	Counter electrode
CV	Cyclic voltammetry
DI	Deionized
ECSA	Electrochemical active surface area
EIS	Electrochemical impedance spectroscopy
FPS	Frames per second
H_2	Hydrogen
HER	Hydrogen evolution reaction
KOH	Potassium hydroxide
LSV	Linear sweep voltammetry
Ni	Nickel
NO_x	Nitrogen oxides
OER	Oxygen evolution reaction
O_2	Oxygen
Pt	Platinum
RE	Reference electrode
RHE	Reversible hydrogen electrode
SMR	Steam methane reforming
SS	Stainless steel
TiO_2	Titanium dioxide
WE	Working electrode
Glossary	
Cdl	Double-layer capacitance (mF cm^{-2})
r	Circle radius
R_a	Average roughness (nm)
r_b	Bubble radius
Rct	Charge transfer resistance (Ω)
S	Surface area (nm^2)
t_b	Growth time
U_0	Peak voltage (V)
U_1	Valley voltage (V)
ΔU	Voltage fluctuation
η	Overpotential (mV)